Quantum Plasmon Resonances Controlled by Molecular Tunnel Junctions

Shu Fen Tan *et al.*

Science **343**, 1496 (2014);
DOI: 10.1126/science.1248797

Science (print ISSN 0036-8075; online ISSN 1095-9203) is published weekly, except the last week in December, by the American Association for the Advancement of Science, 1200 New York Avenue NW, Washington, DC 20005.

and the fluid (Fig. 4C). Unlike autocorrelation, which by definition is time-symmetric, $C_{vF_{th}}(\tau)$ is different for positive and negative τ. The existence of nonzero correlation between the velocity and the thermal force exerted on the bead at future times may seem counterintuitive. This too is a consequence of the hydrodynamic interactions. In the Ornstein-Uhlenbeck model it is exactly zero for $\tau > 0$; the velocity contains no information about future thermal force. Nonzero correlation for positive τ does not violate causality, however. The thermal force of the future is correlated to the thermal force of the past (Fig. 4B), and the velocity is correlated to the thermal force of the past, resulting in nonzero correlation between velocity and the future force (*27*).

Pushing the limits of detection has allowed us to resolve the trajectory in velocity space of Brownian particles in liquid, which, in typical experiments, is normally obscured by noise or concealed by averaging. Our measurements confirm a Maxwell-Boltzmann probability distribution for the velocity with the particle mass replaced by an effective mass that accounts for the inertia of the displaced liquid. Our observations agree with the predicted effects of hydrodynamic interactions on Brownian dynamics, including a faster-than-exponential decay of the VACF and correlations in time of the random thermal force. Our techniques will find broad applications in the study of non-Newtonian fluids (*28*), effects of hydrodynamic interactions in confined geometries (*29*), and nonequilibrium statistical mechanics (*30*, *31*).

References and Notes

1. A. Einstein, *Ann. Phys.* **322**, 549–560 (1905).
2. J. Perrin, *Ann. Chim. Phys.* **18**, 5–104 (1909).
3. M. Kerker, *J. Chem. Educ.* **51**, 764 (1974).
4. A. Einstein, *Zeitschrift für Elektrotechnik und Elektrochemie* **13**, 41–42 (1907).
5. T. Li, S. Kheifets, D. Medellin, M. G. Raizen, *Science* **328**, 1673–1675 (2010).
6. J. Duplat, S. Kheifets, T. Li, M. G. Raizen, E. Villermaux, *Phys. Rev. E* **87**, 020105 (2013).
7. T. Li, S. Kheifets, M. G. Raizen, *Nat. Phys.* **7**, 527–530 (2011).
8. G. L. Paul, P. N. Pusey, *J. Phys. Math. Gen.* **14**, 3301–3327 (1981).
9. R. F. Fox, *J. Math. Phys.* **18**, 2331 (1977).
10. D. A. Beard, T. Schlick, *J. Chem. Phys.* **112**, 7323 (2000).
11. G. Nägele, P. Baur, *Physica A* **245**, 297–336 (1997).
12. H. Craighead, *Nature* **442**, 387–393 (2006).
13. R. Huang *et al.*, *Nat. Phys.* **7**, 576–580 (2011).
14. T. Franosch *et al.*, *Nature* **478**, 85–88 (2011).
15. R. Kubo, *Rep. Prog. Phys.* **29**, 255–284 (1966).
16. G. E. Uhlenbeck, L. S. Ornstein, *Phys. Rev.* **36**, 823–841 (1930).
17. R. Zwanzig, M. Bixon, *J. Fluid Mech.* **69**, 21–25 (1975).
18. J. Boussinesq, *C. R. Hebd. Seances Acad. Sci.* **100**, 935 (1885).
19. A. B. Basset, *Phys. Eng. Sci.* **179**, 43–63 (1888).
20. E. J. Hinch, *J. Fluid Mech.* **72**, 499 (1975).
21. V. Vladimirsky, Y. Terletzky, *Fiz.* **15**, 258–263 (1945).
22. See supplementary materials on *Science* Online.
23. R. Zwanzig, M. Bixon, *Phys. Rev. A* **2**, 2005–2012 (1970).
24. Y. Kim, J. Matta, *Phys. Rev. Lett.* **31**, 208–211 (1973).
25. B. Alder, T. Wainwright, *Phys. Rev. Lett.* **18**, 988–990 (1967).
26. H. J. Clercx, P. P. Schram, *Phys. Rev. A* **46**, 1942–1950 (1992).
27. R. E. London, *J. Chem. Phys.* **66**, 471 (1977).
28. M. Grimm, S. Jeney, T. Franosch, *Soft Matter* **7**, 2076 (2011).
29. B. U. Felderhof, *J. Chem. Phys.* **123**, 184903 (2005).
30. G. M. Wang, E. M. Sevick, E. Mittag, D. J. Searles, D. J. Evans, *Phys. Rev. Lett.* **89**, 050601 (2002).
31. D. Rings, R. Schachoff, M. Selmke, F. Cichos, K. Kroy, *Phys. Rev. Lett.* **105**, 090604 (2010).

Acknowledgments: M.G.R. acknowledges support from the Sid W. Richardson Foundation and the R. A. Welch Foundation (grant F-1258). All raw data and analysis code used to generate results presented in this work are available upon request to M.G.R.

Supplementary Materials

www.sciencemag.org/content/343/6178/1493/suppl/DC1
Materials and Methods
Supplementary Text
Figs. S1 to S3
References (*32*–*35*)

5 November 2013; accepted 20 February 2014
10.1126/science.1248091

Quantum Plasmon Resonances Controlled by Molecular Tunnel Junctions

Shu Fen Tan,[1] Lin Wu,[2] Joel K.W. Yang,[3,4] Ping Bai,*[2] Michel Bosman,*[3] Christian A. Nijhuis*[1,3,5,6]

Quantum tunneling between two plasmonic resonators links nonlinear quantum optics with terahertz nanoelectronics. We describe the direct observation of and control over quantum plasmon resonances at length scales in the range 0.4 to 1.3 nanometers across molecular tunnel junctions made of two plasmonic resonators bridged by self-assembled monolayers (SAMs). The tunnel barrier width and height are controlled by the properties of the molecules. Using electron energy-loss spectroscopy, we directly observe a plasmon mode, the tunneling charge transfer plasmon, whose frequency (ranging from 140 to 245 terahertz) is dependent on the molecules bridging the gaps.

Quantum mechanical effects in plasmonic structures are believed to become important when two plasmonic resonators are placed so closely that electrons can tunnel across the gap (*1*–*11*). Direct experimental access to the resulting tunneling charge transfer plasmon (tCTP) mode is expected to open up new opportunities in, for instance, nanoscale optoelectronics, single-molecule sensing, and nonlinear optics (*1*). Experimental and theoretical studies so far have concluded that quantum mechanical effects are important only at length scales below 0.3 to 0.5 nm, close to the bond length of gold and silver (*8*–*11*). Such structures are technologically inaccessible; therefore, it is important to demonstrate the tCTP mode across gaps larger than a nanometer that can be fabricated by state-of-the-art fabrication techniques (*10*). Unlike past works that investigated tunneling through a vacuum (*12*), we placed molecules in the gap because tunneling rates across molecules depend on the molecular structure and are much higher than across a vacuum. This approach made it possible to directly observe and control tCTPs experimentally in tunneling gaps up to at least 1.3 nm, depending on the type of molecules bridging the gap, and to move quantum plasmonics into the size domain that is accessible via bottom-up or top-down fabrication methods (*10*).

Quantum effects have been observed only indirectly as shifts in the bonding dipolar resonance plasmon mode (*1*, *9*, *11*). Our aim was to perform an experiment in which the presence of a tunneling barrier can be directly imaged while the tCTP mode is simultaneously measured spectroscopically by introducing two experimental innovations: The cross-sectional area of the tunnel junction was increased from a few nm^2 to roughly 10^3 nm^2, and the tunneling rate across the nanogaps was increased by tunneling through molecules rather than vacuum.

Cuboidal silver nanoparticles were used (*13*), separated by SAMs with thicknesses of 0.5 to 0.6 nm forming metal-SAM-metal junctions through self-assembly (Fig. 1). The facets of the nanoparticles are atomically flat, which results in a very large cross-sectional area of around 10^3 nm^2, maximizing the number of tunneling events across the junctions. The silver nanoparticles were functionalized with either saturated, aliphatic 1,2-ethanedithiolates (EDT) or aromatic 1,4-benzenedithiolates (BDT) (*14*). The lengths of EDT and BDT are similar, but they have very different HOMO (highest occupied

[1]Department of Chemistry, National University of Singapore, 3 Science Drive 3, Singapore 117543, Singapore. [2]Institute of High Performance Computing, A*STAR (Agency for Science, Technology and Research), 1 Fusionopolis Way, 16-16 Connexis North, Singapore 138632, Singapore. [3]Institute of Materials Research and Engineering, A*STAR, 3 Research Link, Singapore 117602, Singapore. [4]Singapore University of Technology and Design, 20 Dover Drive, Singapore 138682, Singapore. [5]Graphene Research Center, National University of Singapore, 2 Science Drive 3, Singapore 117542, Singapore. [6]Solar Energy Research Institute of Singapore (SERIS), National University of Singapore, Singapore 117574, Singapore.

*Corresponding author. E-mail: baiping@ihpc.a-star.edu.sg (P.B.), michel.bosman@gmail.com (M.B.), christian.nijhuis@nus.edu.sg (C.A.N.)

molecular orbital)–LUMO (lowest unoccupied molecular orbital) gaps of 8 and 5 eV, respectively (*15*–*17*). Therefore, the tunneling rates across junctions with BDT molecules are higher than those junctions with EDT. The interaction between the two nanoparticles was optimized to avoid aggregation or misalignment by diluting the dithiols with 1-propanethiol (PT) (*14*). After self-assembly of the dimeric structures, they were deposited on a 30-nm-thick, electron-transparent silicon nitride membrane.

A simplified form of the Simmons equation (Eq. 1) is commonly used to approximate molecular tunnel junctions (*18*, *19*)

$$J = J_0 e^{-\beta d}$$

with

$$\beta = 2\sqrt{\frac{2m\varphi}{\hbar^2}} \qquad (1)$$

where β ($Å^{-1}$) is the tunneling decay coefficient, d (nm) is the width of the tunneling barrier, and the pre-exponential factor J_0 (A/cm^2) is the hypothetical current when $d = 0$; m is the mass of the charge carrier (kg), and $\hbar$ is the reduced Plank's constant. The value of β depends on the barrier height φ (eV). Tunneling rates through molecular bonds, so-called through-bond tunneling, are much higher (β ≈ 0.8 to 0.9 $Å^{-1}$ for saturated molecules and 0.1 to 0.3 $Å^{-1}$ for unsaturated molecules) than through vacuum (β = 2.9 $Å^{-1}$) (*20*). Figure 1C shows the energy level diagram of the metal-SAM-metal junctions schematically. As indicated in Fig. 1C, in molecular electronics d is defined by the length of the molecule d_l (nm), and φ by the offset between the Fermi levels of the metal and the energy level of the molecular frontier orbitals. In contrast, when tunneling through a vacuum is the dominant mechanism of charge transport, the barrier height equals the work function of the electrode materials and d equals the gap, d_g (nm), between the two electrodes—that is, the distance between the nanoparticles (*21*).

Instead of bringing the dimer particles in contact with electrical probes that will perturb the plasmon resonances, we used in our experiment a focused beam of energetic electrons in a scanning transmission electron microscope (STEM) as a contactless nanoprobe to excite and analyze the surface plasmon resonances in individual dimers. We positioned the electron probe opposite the gap at the long axis of a silver particle dimer, as illustrated in Fig. 1A, to excite plasmon modes—similar to lateral plane wave illumination of the dimer (*14*). During the plasmon excitation, the tunnel junction was therefore not exposed to the electron beam to minimize irradiation damage (*14*). The excitation of plasmon resonances results in an energy transfer from the electron beam to the particle system, which we analyzed with monochromated electron energy-loss spectroscopy (EELS) (*22*–*24*). The junctions were imaged before and after acquiring the EELS spectra to ensure that none of these junctions formed conductive metal filaments during the experiment (*14*). Thus, in all of our experiments, we could discriminate between the tunneling and conduction through metal filaments—CTP modes conclusively.

Figure 2A shows atomic-resolution TEM images of a silver nanoparticle dimer. The first peak in the histograms of values of d_g estimated from TEM images on a series of dimers is centered at 0.55 ± 0.08 nm for EDT and 0.67 ± 0.12 nm for BDT, which are close to d_l as expected for Ag-SAM-Ag structures. The second peak in these histograms is attributed to dimers with SAMs on both nanoparticles (Ag-SAM//SAM-Ag structures, where "//" indicates a noncovalent contact). Intercalating SAMs or incompletely removed polymer that was used in the nanoparticle synthesis may result in smaller and larger gap sizes than expected from the molecular lengths, as indicated schematically in Fig. 3.

Figure 2B shows EELS spectra recorded from junctions with SAMs of EDT and BDT. Three main plasmon peaks were observed around 2.2 eV, 3.2 eV, and 3.6 eV, which we assigned to the bonding dipolar plasmon mode (II), the transverse corner mode (III), and the transverse edge mode (IV), respectively, in agreement with the finite-element-model (FEM) simulations (Fig. 2D) (*14*, *21*). A new low-energy plasmon mode is observed at 0.60 ± 0.04 eV for EDT and 1.01 ± 0.01 eV for BDT.

We assigned this plasmon mode to the tCTP based on our calculations that show the transfer of net charge between the cuboids (Fig. 2D, mode I). The plasmon resonances of the Ag-SAM-Ag system was simulated using a quantum-corrected FEM optical simulation model (*14*, *21*). Briefly, the optical properties of the junctions are calculated through a quantum mechanical approach and then used to simulate the plasmon resonances of the Ag-SAM-Ag system. The model predicts that the tCTP mode strongly depends on φ, d, and gap field, E_{gap} (V/m). The value of φ is modeled analytically as $\varphi = \alpha E_{HL}$, where $0 < \alpha < 1$ relates to the energy-level alignment, and E_{HL} is the HOMO-LUMO gap, which was obtained from single-molecule experiments (*15*–*17*). We assume $E_{gap} = 7 \times 10^8$ V/m throughout the calculations based on previously reported work (*14*, *21*).

The nature of the charge transport—through-space or through-bond tunneling—was determined from EELS measurements on 32 junctions, for which the energy of the tCTP mode was plotted as a function of d_g (Fig. 2C). This graph shows that the tCTP depends only weakly on the value of d_g. The dotted lines in Fig. 2C show simulations of the tCTP energy shifts if through-space tunneling dominated, with $d = d_g$ (*14*). The solid lines are simulations for through-bond tunneling with $d = d_l$, where the through-bond tunneling distance depends on the length of the molecule and can be different from d_g when the molecules are not perfectly aligned in the gap. Figure 2C shows that through-bond tunneling has a much weaker dependence on gap size than through-space tunneling. The good agreement with the experimental results indicates that coherent through-bond tunneling is the dominant mechanism of charge transport (*14*).

Through-bond tunneling allows us to explore the tCTP mode across a large gap because the tunneling is less dependent on the gap size. EELS spectra were recorded on Ag-SAM//SAM-Ag junctions to study whether the tCTP mode could be observed over larger length scales up to 1.3 nm. Figure 3 shows a tCTP mode for the structures with BDT at 0.975 to 1.015 eV. The tCTP peak energy only weakly depends on d_g, which confirms

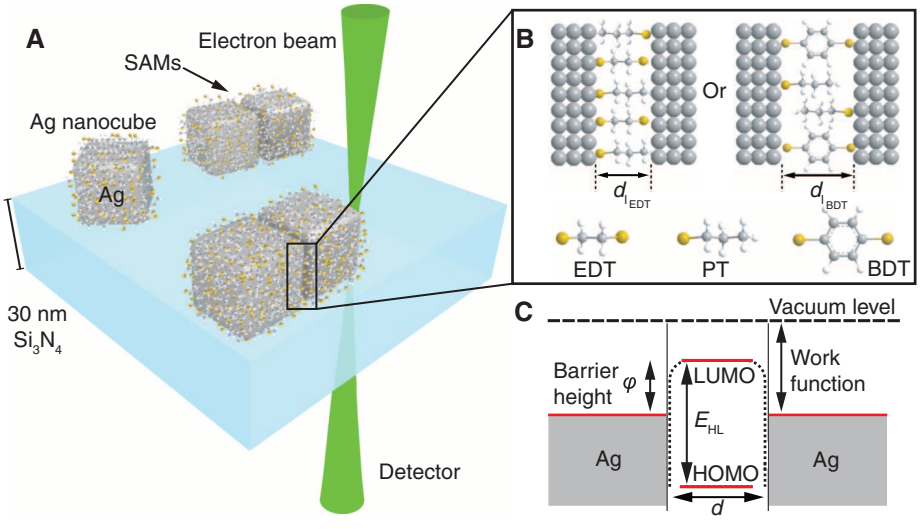

Fig. 1. Quantum plasmonic tunnel junctions. (**A**) Schematic illustration of the molecular tunnel junctions made of two silver nanoparticles bridged by a SAM on an electron-transparent silicon nitride membrane. The contactless electron nanoprobe was placed near the functionalized silver nanoparticles to excite and measure the surface plasmons of individual dimers. (**B**) The distance between two adjacent nanoparticles is determined by the thickness of the SAMs of EDT or BDT. (**C**) A schematic energy-level diagram of the junctions.

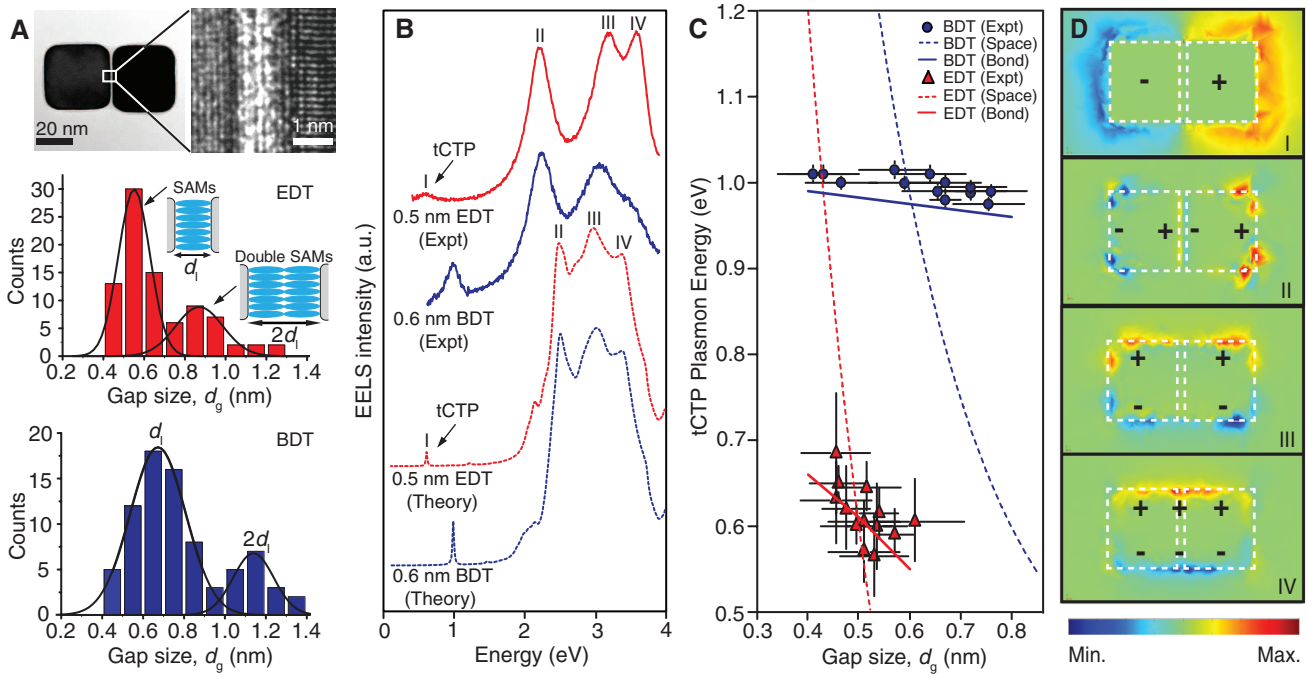

Fig. 2. Direct observation of quantum tunneling between plasmon resonators. (**A**) A high-resolution TEM image of the junctions and histograms of the gap-sizes (*14*). (**B**) Two examples of measured EELS spectra with the occurrence of quantum tunneling directly observed by the tCTP peak and quantum-corrected simulations of the extinction spectra, confirming the identification of the peaks. (**C**) Experimentally measured plasmon energy as a function of gap size for dimers functionalized with monolayers of BDT (blue circles) and EDT (red triangles). Theoretical calculations for through-space and through-bond tunneling are shown as dotted lines and solid lines, respectively, for the two SAMs. (**D**) Simulated maps of the electrical-field distributions for the plasmon modes I to IV, corresponding with the spectral peaks.

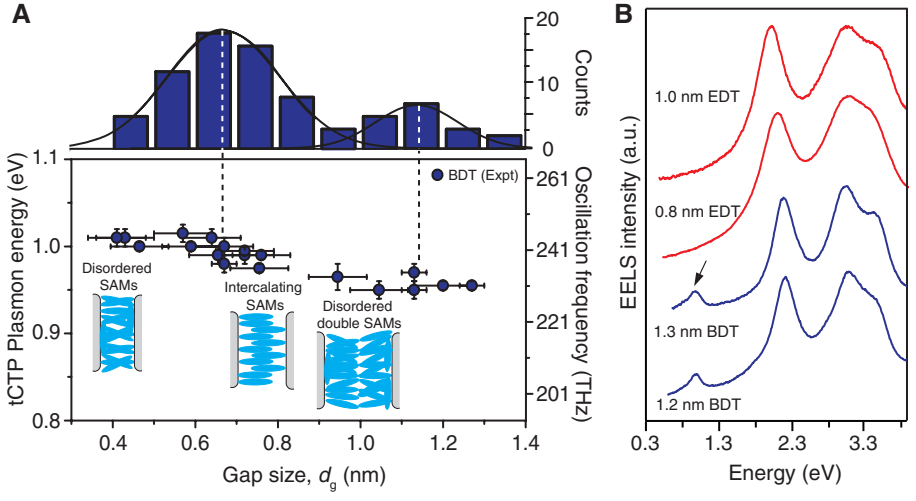

Fig. 3. Quantum plasmon resonances as a function of tunneling distance. (**A**) Experimentally measured plasmon energy as a function of gap size for BDT- (blue circles) functionalized dimers. The gap size varies between individual dimers because of structural disorder in the SAMs. (**B**) Measured EELS spectra for double SAMs of EDT (red) and BDT (blue). Tunneling was observed for the double-layer BDT but not in the double-layer EDT junctions.

that though-bond tunneling is the dominant mechanism of charge transport. The marginal difference in energy of the tCTP mode for single and double SAMs is likely due to strong π–π coupling between the BDT SAMs (*25*). For Ag-SAM//SAM-Ag structures with EDT, the tCTP mode was not observed because of the low β value, and because no π–π coupling occurs between aliphatic molecules, we expected its peak—if any—to be at very low energies below the detection limit of our instrument.

By combining atomic-resolution imaging, single-particle spectroscopy, and monolayer molecular control, we have demonstrated quantum-mechanical electron tunneling at optical frequencies between plasmon resonators. By varying the self-assembled molecular monolayers in the junctions, we found that the plasmon-induced tunneling frequencies could be controlled from 1.01 ± 0.01 eV, or 244 ± 3 THz, for a monolayer of BDT molecules, to 0.60 ± 0.04 eV, or 145 ± 10 THz, for a monolayer of EDT molecules. The mechanism of charge transport was coherent through-bond tunneling, which is only weakly dependent on the gap size. The relatively large distance of up to 1.3 nm over which the tunneling takes place in Ag-BDT//BDT-Ag junctions may provide potential for molecular control over quantum plasmonic systems through longer molecules to perhaps 4 to 5 nm (*26*)—that is, gap sizes that are currently accessible by top-down fabrication techniques. Our results show that tunneling can reconcile molecular electronics with plasmonics, opening up a whole new interdisciplinary field of exploration.

References and Notes

1. M. S. Tame *et al.*, *Nat. Phys.* **9**, 329–340 (2013).
2. M. L. Brongersma, V. M. Shalaev, *Science* **328**, 440–441 (2010).
3. I. Romero, J. Aizpurua, G. W. Bryant, F. J. García De Abajo, *Opt. Express* **14**, 9988–9999 (2006).
4. J. Zuloaga, E. Prodan, P. Nordlander, *Nano Lett.* **9**, 887–891 (2009).
5. D. C. Marinica, A. K. Kazansky, P. Nordlander, J. Aizpurua, A. G. Borisov, *Nano Lett.* **12**, 1333–1339 (2012).
6. P. Song, P. Nordlander, S. Gao, *J. Chem. Phys.* **134**, 074701 (2011).
7. J. Kern *et al.*, *Nano Lett.* **12**, 5504–5509 (2012).
8. R. Esteban, A. G. Borisov, P. Nordlander, J. Aizpurua, *Nat. Commun.* **3**, 825 (2012).
9. J. A. Scholl, A. García-Etxarri, A. L. Koh, J. A. Dionne, *Nano Lett.* **13**, 564–569 (2013).
10. H. Duan, A. I. Fernández-Domínguez, M. Bosman, S. A. Maier, J. K. W. Yang, *Nano Lett.* **12**, 1683–1689 (2012).

11. K. J. Savage *et al.*, *Nature* **491**, 574–577 (2012).
12. C. Ciracì *et al.*, *Science* **337**, 1072–1074 (2012).
13. J. Henzie, S. C. Andrews, X. Y. Ling, Z. Li, P. Yang, *Proc. Natl. Acad. Sci. U.S.A.* **110**, 6640–6645 (2013).
14. See supplementary materials on *Science* Online.
15. A. Salomon *et al.*, *Adv. Mater.* **15**, 1881–1890 (2003).
16. M. A. Reed, C. Zhou, C. J. Muller, T. P. Burgin, J. M. Tour, *Science* **278**, 252–254 (1997).
17. X. D. Cui *et al.*, *J. Phys. Chem. B* **106**, 8609–8614 (2002).
18. C. A. Nijhuis, W. F. Reus, J. B. Barber, G. M. Whitesides, *J. Phys. Chem. C* **116**, 14139–14150 (2012).
19. C. Joachim, M. A. Ratner, *Proc. Natl. Acad. Sci. U.S.A.* **102**, 8801–8808 (2005).
20. R. L. McCreery, *Chem. Mater.* **16**, 4477–4496 (2004).
21. L. Wu *et al.*, *ACS Nano* **7**, 707–716 (2013).
22. J. Nelayah *et al.*, *Nat. Phys.* **3**, 348–353 (2007).
23. M. Bosman, V. J. Keast, M. Watanabe, A. I. Maaroof, M. B. Cortie, *Nanotechnology* **18**, 165505 (2007).
24. M. Bosman *et al.*, *Sci. Rep.* **3**, 1312 (2013).
25. S. Wu *et al.*, *Nat. Nanotechnol.* **3**, 569–574 (2008).
26. S. H. Choi, B. Kim, C. D. Frisbie, *Science* **320**, 1482–1486 (2008).

Acknowledgments: We acknowledge the National Research Foundation (NRF) for supporting this research under the Competitive Research Programme (CRP) program (award NRF-CRP 8-2011-07). J.K.W.Y, P.B., and L.W. acknowledge the Agency for Science, Technology and Research (A*STAR) for the A*STAR Investigatorship Grant, and TSRP grant 1021520014.

Supplementary Materials

www.sciencemag.org/content/343/6178/1496/suppl/DC1
Materials and Methods
Supplementary Text
Figs. S1 to S11
References (*27*–*40*)

21 November 2013; accepted 28 February 2014
10.1126/science.1248797

Optical Broadband Angular Selectivity

Yichen Shen,[1]* Dexin Ye,[2] Ivan Celanovic,[1] Steven G. Johnson,[1,3] John D. Joannopoulos,[1] Marin Soljačić[1]

Light selection based purely on the angle of propagation is a long-standing scientific challenge. In angularly selective systems, however, the transmission of light usually also depends on the light frequency. We tailored the overlap of the band gaps of multiple one-dimensional photonic crystals, each with a different periodicity, in such a way as to preserve the characteristic Brewster modes across a broadband spectrum. We provide theory as well as an experimental realization with an all–visible spectrum, p-polarized angularly selective material system. Our method enables transparency throughout the visible spectrum at one angle—the generalized Brewster angle—and reflection at every other viewing angle.

The ability to control light has long been a major scientific and technological goal. In electromagnetic theory, a monochromatic electromagnetic plane wave is characterized (apart from its phase and amplitude) by three fundamental properties: its frequency, its polarization, and its propagation direction. The ability to select light according to each of these separate properties would be an essential step in achieving control over light (Fig. 1).

Tremendous progress has been made toward both frequency selectivity and polarization selectivity. Frequency selectivity (Fig. 1A) can be obtained, for example, by taking advantage of photonic band gaps in photonic crystals (*1*–*5*). Polarization selectivity (Fig. 1B) is accomplished, for example, by means of a "wire grid" polarizer (*6*) or by exploiting birefringent materials (*7*, *8*). Methods based on interference and resonance effects have been explored for angular selectivity, but they have limited applications because they are sensitive to frequency.

An angularly selective material system should ideally work over a broadband spectrum. Such a system could potentially play a crucial role in many applications, such as high-efficiency solar energy conversion (*9*, *10*), privacy protection (*11*), and detectors with high signal-to-noise ratios. Some progress has been made toward achieving broadband angular selectivity by means of metallic extraordinary transmission (*12*, *13*), anisotropic metamaterials (*14*), combined use of polarizers and birefringent films (*11*), or geometrical optics at micrometer scale (*15*). The first two of these mechanisms are difficult to realize in the optical regime; the other two work only as angularly selective absorbers.

Here, we introduce a basic principle to achieve optical broadband angular selectivity. Our result rests on (i) the fact that polarized light transmits without any reflection at the Brewster angle, (ii) the existence in photonic crystals of band gaps that prevent light propagation for given frequency ranges, and (iii) the band gap–broadening effect of heterostructures. First, we prove our fundamental idea theoretically for a single polarization and oblique incident angles, and also for both polarizations and normal angle of incidence. Second, we experimentally demonstrate the concept in the case of all–visible spectrum, p-polarized light. The demonstrator is transparent for all colors at one viewing angle and highly reflecting at every other viewing angle.

We begin by considering a simple quarter-wave stack with periodicity a, relative permeability μ of $\mu_1 = \mu_2 = 1$, and relative permittivities ε of ε_1 and ε_2. In such a system, monochromatic plane waves with frequency ω propagate only in certain directions; propagation in other directions is not allowed because of destructive interference (*3*). Another way to look at this is through the photonic band diagram shown in Fig. 2A: Modes that are allowed to propagate (so-called extended modes) exist in the shaded region; no modes are allowed to propagate in the white regions (known as band gaps). In the photonic band diagram, modes with propagation direction forming an angle θ_i with respect to the z axis in Fig. 2 (in the layers with dielectric constant ε_i) lie on a straight line represented by $\omega = k_y c/(\sqrt{\varepsilon_i}\sin\theta_i)$, where k_y is the y component (as defined in Fig. 2) of the wave vector $\mathbf{k}$ and c is the speed of light; for general propagation angle θ_i, this line will extend through the regions of the extended modes as well as through the band gap regions.

However, for p-polarized light, there is a special propagation angle, known as the Brewster angle θ_B, for which the extended modes exist regardless of ω (dashed line in Fig. 2A) (*8*, *16*):

$$\theta_B = \tan^{-1}\sqrt{\frac{\varepsilon_2}{\varepsilon_1}} \quad (1)$$

where θ_B is the Brewster angle in the layers with dielectric constant ε_1. At θ_B, p-polarized light is fully transmitted for all frequencies at both interfaces (from ε_1 to ε_2 layers and from ε_2 to ε_1 layers). This condition is not sufficient to achieve angular selectivity; we also need to remove all the extended modes in other propagation directions. Because the location of the band gap scales proportionally to the periodicity of the quarter-wave stack, the effective band gap can be enlarged when we stack quarter-wave stacks with various periodicities together (*17*–*19*). The details of this process are illustrated in fig. S1 (*20*). As a proof of principle, in Fig. 2D we plot the band diagram of an ideal structure with $\varepsilon_1 = 1$ and $\varepsilon_2 = 2$ and the number of quarter-wave stacks approaching infinity. By doing this with a finite system of 50 stacks (10 bilayers in each stack), we can achieve an angularly selective range of less than 2° and a frequency bandwidth of ≥54%, similar to the size of the visible spectrum (Fig. 2G).

For s-polarized light, as there is no Brewster angle, this construction behaves as a dielectric mirror that reflects over a wide frequency range and over all incident angles (fig. S2) (*20*).

The mechanism above provides both angular selectivity and polarization selectivity, and is therefore useful in many applications. For example, in most optically pumped lasers, the pumping light comes in with a specific polarization and at one specific angle. A cavity built with both angularly selective and polarization-selective mirrors will allow the pumping light to get through, while at the same time trapping all the light with other propagation directions and polarizations inside the cavity.

The restriction on the polarization can be lifted by releasing the conventional requirement that $\mu_1 = \mu_2 = 1$. During the past decade, it has been demonstrated that metamaterials have the potential to achieve $\varepsilon = \mu \neq 1$ in a broad frequency range (*21*–*23*). Consider two media with $\varepsilon_1 = \mu_1 \neq \varepsilon_2 = \mu_2$;

[1]Research Laboratory of Electronics, Massachusetts Institute of Technology, Cambridge, MA 02139, USA. [2]Laboratory of Applied Research on Electromagnetics, Zhejiang University, Hangzhou 310027, China. [3]Department of Mathematics, Massachusetts Institute of Technology, Cambridge, MA 02139, USA.
*Corresponding author. E-mail: ycshen@mit.edu